Journal of Aviation and Space Studies
Havacılık ve Uzay Çalışmaları Dergisi

E-ISSN: 2757-7317 & URL: https://dergipark.org.tr/pub/jass

Theoretical Paper

Aerodynamic performance analysis of NACA 0015 airfoil at low Reynolds numbers

Mustafa Buğday[1]

Abstract. This study aims to enhance the aerodynamic performance of a NACA 0015 series symmetric airfoil. The research was conducted using the Ansys Fluid Flow (CFD) module. The analysis area comprised 300,000 mesh elements. Several comparative analyses were conducted at low Reynold number (Re) and angles of attack ranging from α=-100 to 100. An increase in the angle of attack typically led to an elevation in the aerodynamic force coefficients (C_l, C_d, and C_l/C_d). In our study, the optimal values were attained at α=80, utilizing the Spalart-Allmaras turbulence model and Re=1×10^6, in comparison with analogous studies in literature. A 30% increase in lift coefficient (C_l) was attained relative to the initial condition. Furthermore, owing to the pressure differential between the lower and upper surfaces of the wing profile, the average velocity values recorded were 29.6 m/s and 18.1 m/s, respectively. Consistent with these findings, it is believed that this series, particularly favored in wind turbines, may operate more efficiently and effectively in the future with the test data acquired from experimental settings.

Keywords: Airfoil, NACA 0015, Ansys, CFD.

Teorik Makale

NACA 0015 kanat profilinin düşük Reynolds sayılarında aerodinamik performans analizi

Öz. Bu çalışma, NACA 0015 serisi simetrik bir kanat profilinin aerodinamik performansını artırmayı amaçlamaktadır. Araştırma, Ansys Fluid Flow (CFD) modülü kullanılarak yürütülmüştür. Analiz alanı 300.000 mesh elemandan oluşmaktadır. Birkaç karşılaştırmalı analiz, düşük Reynolds sayılarında ve α=-10^0 ile 10^0 arasında değişen hücum açılarında gerçekleştirilmiştir. Hücum açısındaki bir artış genellikle aerodinamik kuvvet katsayılarında (C_l, C_d ve C_l/C_d) bir yükselmeye yol açmıştır. Çalışmamızda, literatürdeki benzer çalışmalarla karşılaştırıldığında, Spalart-Allmaras türbülans modeli ve Re=1×10^6 kullanılarak α=80^0'de optimum değerlere ulaşılmıştır. Başlangıç koşuluna göre kaldırma katsayısında (C_l) %30'luk bir artış elde edilmiştir. Ayrıca kanat profilinin alt ve üst yüzeyleri arasındaki basınç farkından dolayı kaydedilen ortalama hız değerleri sırasıyla 29,6 m/s ve 18,1 m/s olmuştur. Bu bulgularla tutarlı olarak, özellikle rüzgâr türbinlerinde tercih edilen bu serinin, deneysel ortamlardan elde edilen test verileriyle gelecekte daha verimli ve etkili çalışabileceği düşünülmektedir.

Anahtar Kelimeler: Kanat profili, NACA 0015, Ansys, CFD.

1 Department of Mechanical Engineering, Karabuk University, 78000, Karabük, Türkiye; mustafabugday@karabuk.edu.tr (Corresponding Author)
https://doi.org/10.52995/jass.1619615
Received: January 14, 2025; Accepted: February 12, 2025; Published: February 28, 2025

1. INTRODUCTION

Airfoils are crucial elements in numerous applications, especially in wind turbine design and aviation, as they directly affect aerodynamic performance, efficiency, and overall functionality. The design and optimization of airfoils entail a complex interaction of geometric parameters, flow characteristics, and operational conditions. A principal factor in airfoil design is the lift-to-drag ratio (L/D ratio), an essential performance metric. A high lift-to-drag (L/D) ratio signifies that an airfoil can produce substantial lift while reducing drag, thereby improving the efficiency of aircraft and wind turbines (Feng, 2023). Optimizing airfoil geometries to attain an ideal lift-to-drag ratio is crucial for enhancing performance. Diverse techniques, such as genetic algorithms and response surface methodologies, have been utilized to optimize airfoil designs, facilitating customized aerodynamic properties that satisfy operational criteria (He & Agarwal, 2014), (Sun, 2011). The selection of airfoil in wind turbines can profoundly influence the turbine's efficiency and power output (He & Agarwal, 2014), (Li, et al., 2018). The design process frequently utilizes sophisticated computational methods, including Ansys CFD software, to analyze and optimize airfoil configurations based on aerodynamic efficiency (Berger, Raffeiner, Senfter, & Pillei, 2024), (Tanürün, Akın, Acır, & Şahin, 2024). Furthermore, the incorporation of advanced design methodologies, including inverse airfoil design techniques, has surfaced as a viable strategy to improve airfoil performance. These methods facilitate the exact customization of airfoil geometries to attain specific aerodynamic properties, especially in low-speed contexts such as Darrieus-type vertical axis wind turbines (Saeed, Paraschivoiu, Trifu, Hess, & Gabrys, 2011). Computational fluid dynamics (CFD) and experimental validation are essential for evaluating the efficiency of these designs (Gopalarathnam & Selig, 2001).

The 4-digit NACA airfoils, including the NACA 0015 and NACA 4412, are defined by their thickness and chamber, which affect lift and drag properties. The NACA 0015 airfoil is extensively analyzed due to its symmetrical design, which provides a consistent lift-to-drag ratio across multiple angles of attack, rendering it appropriate for diverse applications, such as small wind turbines and general aviation aircraft (Abramova, Alieva, Sudakov, & Khrabrov, 2024), (Hassan, Andan, Asrar, & Sapardi, 2023). The NACA 4412, featuring a cambered configuration, offers improved lift properties, especially at reduced velocities, advantageous for scenarios necessitating significant lift during takeoff and landing (Arif, et al., 2022). Recent studies have illustrated the efficacy of NACA airfoils across various operational conditions. Computational fluid dynamics (CFD) analyses indicate that the NACA 0015 airfoil demonstrates advantageous aerodynamic performance, providing substantial insights into the impact of angle of attack variations on lift and drag coefficients (Abramova, Alieva, Sudakov, & Khrabrov, 2024), (Hassan, Andan, Asrar, & Sapardi, 2023). The incorporation of features like morphing trailing edges has been investigated to enhance aerodynamic performance, suggesting that these alterations can result in better lift-to-drag ratios across different flight conditions (Ai, Jawahar, & Azarpeyvand, 2016), (Jawahar, Qing,, & Azarpeyvand, 2018). Experimental validation studies have compared the aerodynamic properties of different NACA airfoils, demonstrating that airfoil thickness and configuration substantially affect stall characteristics and overall performance (Abed, 2023), (Bangga, Hutani, & Heramarwan, 2021). The NACA 0015 airfoil demonstrates effective performance under dynamic stall conditions, essential for vertical axis wind turbine applications (Bangga, Hutani, & Heramarwan, 2021). The incorporation of vortex generators and additional flow control devices has been investigated to improve performance by postponing flow separation and augmenting lift (Bangga, Hutani, & Heramarwan, 2021).

The examination of NACA airfoils at low Re is essential for applications in micro aerial vehicles, unmanned aerial vehicles, and other aerodynamic devices functioning in low-speed environments. Aerodynamics at low Re poses distinct challenges, including flow separation, stall characteristics, and diminished lift-to-drag ratios, which considerably impact the performance of airfoils like the NACA 4415 and NACA 0012. Studies demonstrate that the NACA 4415 airfoil, although efficient at elevated Re, shows inadequate performance at low Re, especially regarding lift and drag properties. Research indicates that at Re as low as 300,000, the lift and drag coefficients of the NACA 4415 are inadequate, resulting in stall problems and diminished aerodynamic efficiency (Ayaz Ümütlü, Kiral, & Karadeniz, 2023), (Julian, Siswanto, Wahyuni, & Bunga, 2023). Experimental investigations substantiate this, revealing the stall behavior of airfoils such as the NACA 2415 and NACA 0015 at Re near 50,000, where considerable flow separation transpires, resulting in a loss of lift (Ayaz Ümütlü, Kiral, & Karadeniz, 2023), (Pack Melton, Hannon, Yao, & Harris, 2008). The aerodynamic efficacy of airfoils at low Re can be improved through diverse modifications and methodologies. The integration of vortex generators has demonstrated enhancement in lift characteristics by postponing flow separation, thereby improving the stall performance of airfoils such as the NACA 4415, as evidenced

in "Lift Enhancement of NACA 4415 Airfoil using Biomimetic Shark Skin Vortex Generator" (Zulkefli, Ahamat, Mohd Safri, Mohd Nur, & Mohd Rafie, 2019). Moreover, research employing computational fluid dynamics (CFD) has shown that refining the geometry of airfoils, including modifications to camber and thickness, can enhance aerodynamic performance at low Re (Hu & Tamai, 2008), (Nepal, Qijun, Bo, Kamruzzaman, & Adhikari, 2023). Ongoing research in this domain is crucial for enhancing the design of efficient airfoils appropriate for low-speed applications.

The examination of turbulence models concerning airfoil performance is essential for comprehending aerodynamic properties and enhancing designs for diverse applications, such as aviation and wind energy. Turbulence considerably impacts the flow surrounding airfoils, affecting lift and drag coefficients, which are essential parameters in aerodynamic performance. Recent studies have employed diverse turbulence models to accurately simulate airflow around airfoils. The study on the NACA 0018 airfoil employed the Spalart-Allmaras turbulence model, demonstrating its efficacy in validating experimental results and analyzing the aerodynamic performance of various airfoil configurations (Kaya, 2024). These findings underscore the necessity of choosing suitable turbulence models to achieve dependable simulations that inform design enhancements. The impact of turbulence on aerodynamic performance is exemplified by Almusawi et al. (Almusawi, Rishack, & Al-fahham, 2022) who discovered that incorporating a semicircular groove on the NACA 0012 airfoil enhanced lift efficiency and diminished drag, highlighting the significance of surface modifications in controlling turbulent flow. Furthermore, research has concentrated on refining established turbulence models, including the Spalart-Allmaras model, to incorporate turbulence energy backscatter, thereby improving the predictive accuracy of simulations related to airfoil interactions with turbulent flows (Liu, Lu, Fang, & Gao, 2011). This alteration is especially pertinent in enhancing airfoil designs for improved performance across diverse flow conditions. The choice and implementation of turbulence models are crucial in the aerodynamic assessment of airfoils. Research consistently demonstrates that effective turbulence modeling can substantially enhance the comprehension and forecasting of airfoil performance in turbulent conditions, thereby informing the design of more efficient aerodynamic structures.

This study examined the aerodynamic performance of the NACA 0015 airfoil at low Re utilizing different turbulence models, specifically the Spalart-Almaras and Standard K-Epsilon models. The results achieved will enhance the efficiency of airfoils utilized in the aviation and renewable energy sectors. Ultimately, a systematic approach to airfoil design, incorporating computer-aided computational techniques and experimental validations, will yield effective and efficient outcomes in meeting the aerodynamic demands of contemporary engineering challenges related to NACA airfoils.

2. METHODS

2.1. Mathematical Model

2.1.1. Continuity equation

For steady-state flows, the continuity equation is expressed as

$$\frac{\partial \rho}{\partial t} + \nabla \cdot (\rho V) = 0. \tag{1}$$

The density as a function of time in the steady state is given as

$$\frac{\partial \rho}{\partial t} = 0. \tag{2}$$

Consequently, the steady-state continuity equation is shown as follows:

$$\frac{\partial}{\partial x}(\rho u) + \frac{\partial}{\partial y}(\rho v) = 0. \tag{3}$$

2.1.2. Momentum equation

For two-dimensional steady flows, the momentum equation is as follows:

$$\vec{\nabla}\cdot\left(\rho u\vec{V}\right) = -\frac{\partial p}{\partial x} + \rho f_x + (f_x)_{\text{viscose}}, \tag{4}$$

$$\vec{\nabla}\cdot\left(\rho v\vec{V}\right) = -\frac{\partial p}{\partial y} + \rho f_y + \left(f_y\right)_{\text{viscose}}, \tag{5}$$

where ρ is density, and f_x and f_y are surface forces.

2.1.3. Energy equation

For the steady state flows, the energy equation is as follows:

$$\vec{\nabla}\cdot\left[\rho\left(e+\frac{V^2}{2}\right)\vec{V}\right] = \rho\dot{q} - \vec{\nabla}\cdot\left(P\vec{V}\right) + \rho\left(\vec{f}\cdot\vec{V}\right) + \dot{Q} + \dot{W}, \tag{6}$$

where the viscous exists and has an impact on the energy equation, as indicated by ($\dot{Q}$) and ($\dot{W}$). A partial differential equation, Eq. (6), links the variables in the flow field at a particular location in space.

2.1.4. Transport equation for the Spalart-Almaras model

The Spalart-Almaras model's transported variable ($\tilde{\gamma}$) yields the following transport equation:

$$\begin{aligned}&\frac{\partial}{\partial t}(\rho\tilde{\gamma}) + \frac{\partial}{\partial x_i}(\rho\tilde{\gamma}u_i) = G_\gamma \\ &+\frac{1}{\sigma_{\tilde{\gamma}}}\left[\frac{\partial}{\partial x_i}\left\{(\mu+\rho\tilde{\gamma})\frac{\partial\tilde{\gamma}}{\partial x_j}\right\} + C_{b2}\rho\left(\frac{\partial\tilde{\gamma}}{\partial x_j}\right)^2\right] - Y_\gamma + S_{\tilde{\gamma}},\end{aligned} \tag{7}$$

where G_γ represents the generation of turbulent viscosity and Y_γ represents the turbulent viscosity destruction that occurs close to the wall because of viscous damping. The constant coefficients, denoted as $C_{b2}$and $\sigma_{\tilde{\gamma}}$ are equivalent to 0.67 and 0.622, respectively. $S_{\tilde{\gamma}}$ is the user-defined source term, and γ is the molecular kinematic viscosity. The turbulent viscosity is calculated using the following equation, which is used to model turbulent viscosity:

$$\mu_t = \rho\tilde{\gamma}f_{v1}, \tag{8}$$

where the viscous damping function, f_{v1}, can be found as follows:

$$f_{v1} = \frac{X^3}{x^3 + C_{v1}^3}, \tag{9}$$

$$X = \frac{\tilde{\gamma}}{\gamma}. \tag{10}$$

The constant coefficient, C_{v1}, is equivalent to 7.1. Using Eqs. (11) and (12), the production term is determined:

$$G_\gamma = C_{b1}\rho\tilde{S}\tilde{\gamma}, \tag{11}$$

$$\tilde{S} \equiv S + \frac{\tilde{\gamma}}{K^2d^2}f_{v2}, \tag{12}$$

which has the constant coefficients C_{b1}=0.1355 and K =0.4187 as $C_{b1}$and K respectively. S is the scalar measure of the deformation tensor, and d is the distance from the wall. The following formulas explain how to determine the turbulent destruction (Y_γ):

$$Y_\gamma = C_{w1}\rho f_w\left(\frac{\tilde{\gamma}}{d}\right)^2, \tag{13}$$

$$f_w = g\left[\frac{1+C_{w3}^6}{g^6+C_{w3}^6}\right]^{1/6}, \tag{14}$$

$$g = r + C_{w2}(r^6 - r), \tag{15}$$

$$r \equiv \frac{\tilde{\gamma}}{\tilde{S}K^2d^2}, \tag{16}$$

where $\tilde{S}$ is derived from Eq. (12) and the constant coefficients are C_{w1}, C_{w2}, and C_{w3}. Additionally, the constant values can be found as:

$$C_{w1} = \frac{C_{b1}}{K^2} + \frac{(1 + C_{b2})}{\sigma_{\tilde{\gamma}}}. \tag{17}$$

After solving the earlier equation, C_{w1} = 3.2059 is found, and C_{w2} and C_{w3} equal 0.3 and 2.0, respectively (Spalart & Allmaras, 1992).

2.1.5. Standard K-Epsilon model

A semi-empirical model (Launder, 1972), the k-ε standard model depends on the kinetic energy of turbulence and how quickly it dissipates. In this model, the flow is assumed to be fully turbulent, and the molecular viscosity may be very small. For turbulent flows, this model is therefore applied. The K-Epsilon model's transport equation is displayed in equations (18) and (19).

$$\frac{\partial}{\partial t}(\rho k) + \frac{\partial}{\partial x_i}(\rho k u_i) = \frac{\partial}{\partial x_i}\left[\left(\mu + \frac{\mu_t}{\sigma_k}\right)\frac{\partial k}{\partial x_j}\right] + G_k + G_b - \rho\varepsilon - Y_M + S_k, \tag{18}$$

$$\frac{\partial}{\partial t}(\rho \varepsilon) + \frac{\partial}{\partial x_i}(\rho \varepsilon u_i) = \frac{\partial}{\partial x_i}\left[\left(\mu + \frac{\mu_t}{\sigma_\varepsilon}\right)\frac{\partial \varepsilon}{\partial x_j}\right] C_{1\varepsilon}\frac{\varepsilon}{k} + (G_k + C_{3\varepsilon}G_b) - C_{2\varepsilon}\rho\frac{\varepsilon^2}{k} + S_\varepsilon, \tag{19}$$

where $Y_M$represents the fluctuating dilation contribution in compressible turbulence and $G_k$represents the turbulent kinetic energy; $C_{1\varepsilon}$ and $C_{2\varepsilon}$are constant coefficients that equal 1.44 and 1.92, respectively; σ_k and $\sigma_\varepsilon$are the turbulent Prandtl numbers for k and ε, which equal 1 and 1.3, respectively. Similarly, μ_t can be found as

$$\mu_t = \rho C_\mu \frac{K^2}{\varepsilon}, \tag{20}$$

where C_μ is equal to 0.09.

2.1.6. Airfoil loads

The pressure coefficient (C_p) is obtained from (Medjroubi, Stoevesandt, Carmo, & Peinke, 2011):

$$C_p \equiv \frac{P - P_\infty}{q_\infty}. \tag{21}$$

The dynamic pressure, q_∞, is found by

$$q_\infty = \frac{1}{2}\rho_\infty V_\infty^2. \tag{22}$$

The following is the dynamic pressure as a function of M_∞:

$$q_\infty = \frac{1}{2}\frac{\gamma q_\infty}{\gamma q_\infty}\rho_\infty V_\infty^2 = \frac{\gamma}{2}P_\infty\left[\frac{\rho_\infty}{\gamma P_\infty}\right]V_\infty^2, \tag{23}$$

and

$$a_\infty^2 = \frac{\gamma P_\infty}{\rho_\infty}. \tag{24}$$

Thus, we obtain q_∞ as follows:

$$q_\infty = \frac{\gamma}{2}P_\infty\frac{V_\infty^2}{a_\infty^2} = \frac{\gamma}{2}P_\infty M_\infty^2. \tag{25}$$

After considering Eqs. (21) and (25), C_p is as follows:

$$C_p = \frac{2}{\gamma M_\infty^2}\left(\frac{P}{P_\infty} - 1\right). \tag{26}$$

Assuming that C is the airfoil's chord and α is the angle of attack, the following values of C_N and C_X are obtained (Li, Sherwin, & Bearman, 2002):

$$C_N = \int_{x=0}^{x=C} \left(C_{P,\text{low}} - C_{P,\text{up}}\right) d\left(\frac{x}{c}\right), \tag{27}$$

$$C_X = \int_{x=0}^{x=C} \left(C_{P,\text{up}}\left(\frac{dY}{dX}\right)_{\text{up}} - C_{P,\text{low}}\left(\frac{dY}{dX}\right)_{\text{low}}\right) d\left(\frac{x}{c}\right). \tag{28}$$

Ultimately, the coefficients of lift and drag are found to be:

$$C_D = C_X \cos\alpha + C_N \sin\alpha, \tag{29}$$

$$C_L = C_N \cos\alpha - C_X \sin\alpha. \tag{30}$$

2.2. Geometry

The coordinates of the NACA 0015 airfoil profile were obtained from the Airfoil Tools (Dell'Orso & Amitay, 2018), (Sato, Asada, Nonomura, Kawai, & Fujii, 2017), (Siauw, et al., 2010). The resultant file was transmitted to the Ansys drawing module to generate the overall geometry of the analysis. The semicircular region preceding the airfoil represents the inlet boundary condition, while the vertical line aligned with the flow direction represents the outlet boundary condition. The dimensions of the drawing geometry are presented in Figure 1.

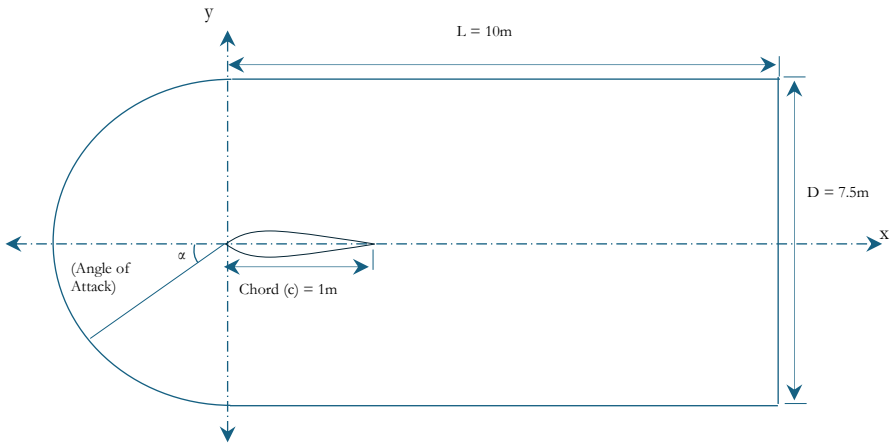

Figure 1. Boundary Domain

2.3. Mesh Independence Test

The same turbulence model (Spalart-Allmaras) and Re= 200,000 were employed to create rectangular meshes with a progressively enhancing mesh configuration to accurately simulate the boundary layer. A mesh convergence study was conducted involving 15 different experiments with mesh elements ranging from 40,000 to 500,000. Figure 2 illustrates the variation of lift and drag coefficients associated with different quantities of mesh elements at an angle of attack of 0°. The illustration indicates that meshes surpassing 300,000 elements yield precise results with minimal variance. Consequently, meshes comprising 300,000 elements were chosen for the ensuing simulations. Figure 3 shows the mesh structure and boundary conditions established within the analysis region.

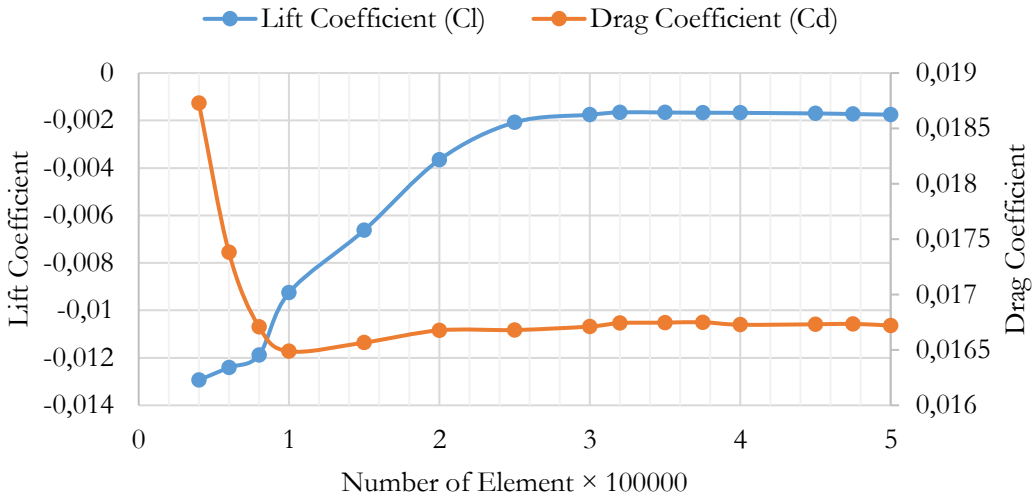

Figure 2. Variation of Lift and Drag Coefficient Depending on the Number of Elements

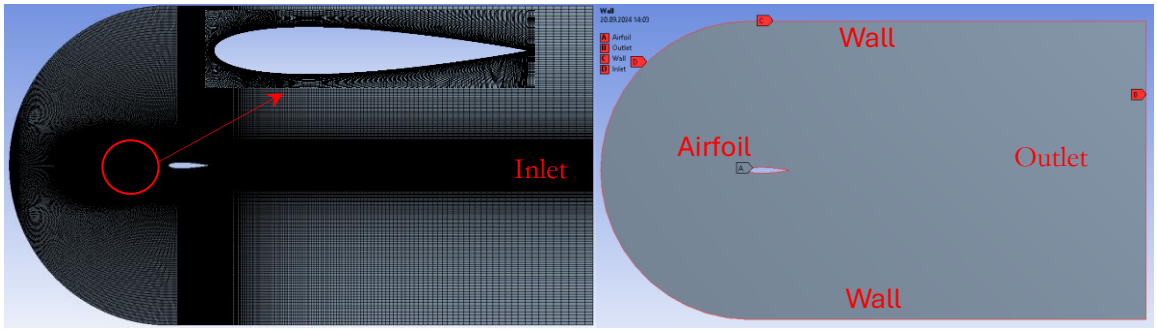

a) b)

Figure 3. a) Mesh Structure b) Boundary Conditions Created in the Analysis Region

2.4. CFD Parameters

The analyses were conducted at low Re of 2×10^5, 4×10^5, 6×10^5, 8×10^5, and 1×10^6, respectively. The turbulence models considered in this study were Spalart-Allmaras and K-Epsilon. Based on the acquired data, the most suitable turbulence model was determined by evaluating their performance. The dynamic viscosity was recorded as 1.789×10^{-5} kg/ms, and the air density was noted as 1.23 kg/m³. The gauge pressure is zero. Ambient atmospheric conditions and no-slip boundary conditions are implemented at the exit and walls, respectively. The geometry of the wing profile is delineated as the wall boundary. When the angle of attack surpasses the stall angle, the K-Epsilon (k-ε) turbulence model, primarily designed for fully developed turbulence, faces limitations in accurately predicting separated flows and is less effective in capturing complex flow separation and reattachment phenomena. Table 1 shows the parameters used in the analysis in detail.

Table 1. CFD Parameters

Boundary Condition	**Type**
Density of Fluid	1.23 kg/m³
Operating Pressure	101325 Pa
Re	2×10^5, 4×10^5, 6×10^5, 8×10^5, 1×10^6
Model	Spalart-Allmaras and K-Epsilon
Viscosity	1.7894×10^{-5} Pa·s
Angle of Attack	-10, 10 step by 1

3. RESULTS AND DISCUSSION

3.1. Validation

The CFD simulation results for the NACA 0015 airfoil closely align with the experimental data from Mazumder (Mazumder, 2024) and Bogateanu (Bogateanu, Dumitrache, Dumitrescu, & Stoica, 2014) for $Re=8\times10^5$ and $Re=1\times10^6$. The simulations precisely align with the experimentally observed trends for the aerodynamic force coefficients (C_l and C_d) across various angles of attack. These comparisons demonstrate that the simulation results are dependable and align with the established experimental findings. The numerical data for $Re=8\times10^5$ and $Re=1\times10^6$, along with the corresponding experimental data, are displayed in Tables 2 and 3 for comparison.

Table 2. Comparison of Aerodynamic Force Coefficients (C_l and C_d) at $Re = 8\times10^5$

	CFD	**Mazumder** (Mazumder, 2024)	**CFD**	**Mazumder** (Mazumder, 2024)
Angel of Attack (α)	**C_l**	**C_l**	**C_d**	**C_d**
-10	-0.9601	-0.9652	0.01533	0.0115
-9	-0.9100	-0.82324	0.01299	0.011
-8	-0.8565	-0.78336	0.01148	0.0105
-7	-0.7809	-0.7865	0.01076	0.01
-6	-0.6831	-0.6798	0.00979	0.0095
-5	-0.5806	-0.5966	0.0088	0.009
-4	-0.4509	-0.4499	0.0079	0.0085
-3	-0.3249	-0.3189	0.0075	0.008
-2	-0.2052	-0.2044	0.00698	0.0075
-1	-0.0998	-0.1006	0.006811	0.007
0	0.0000	0	0.006788	0.0065
1	0.1270	0.1266	0.006811	0.007
2	0.2612	0.2595	0.00698	0.0075
3	0.4136	0.3955	0.0075	0.008
4	0.5739	0.5622	0.0079	0.0085
5	0.7388	0.7022	0.0088	0.009
6	0.8694	0.8465	0.00979	0.0095
7	0.9939	0.9647	0.01076	0.01
8	1.0900	1.108	0.01148	0.0105
9	1.1581	1.1036	0.01299	0.011
10	1.2233	1.2307	0.01533	0.0115

Table 3. Comparison of Aerodynamic Force Coefficients (C_l and C_d) at $Re = 1\times10^6$

	CFD	**Bogateanu** (Bogateanu, Dumitrache, Dumitrescu, & Stoica, 2014)	**CFD**	**Bogateanu** (Bogateanu, Dumitrache, Dumitrescu, & Stoica, 2014)
Angel of Attack (α)	**C_l**	**C_l**	**C_d**	**C_d**
-10	-0.94282	-0.9422	0.01498	0.014325069
-9	-0.882215	-0.86532	0.01355	0.012954761
-8	-0.768315	-0.7566	0.01201	0.011458112
-7	-0.655095	-0.64321	0.01095	0.010165551
-6	-0.54655	-0.52334	0.0095	0.008950739

-5	-0.45594	-0.46258	0.0086	0.007988607
-4	-0.36788	-0.35632	0.0078	0.00719169
-3	-0.277185	-0.26591	0.00693	0.00667661
-2	-0.185215	-0.18643	0.00684	0.006346181
-1	-0.092735	-0.10103	0.00644	0.006180966
0	0	0	0.0064	0.006142092
1	0.125465	0.1233	0.00644	0.006820853
2	0.250585	0.2533	0.00684	0.0070142
3	0.3749	0.3699	0.00693	0.007379411
4	0.49772	0.48996	0.0078	0.00794871
5	0.61686	0.62077	0.0086	0.008829513
6	0.739565	0.70956	0.0095	0.009892922
7	0.88642	0.88951	0.01095	0.011235609
8	1.0396	1.0261	0.01201	0.012664229
9	1.193815	1.2014	0.01355	0.01431842
10	1.275465	1.28067	0.015833	0.01582223

3.2. Results

3.2.1. Aerodynamic forces

The aerodynamic force coefficients of NACA 0015 at variable Re=200,000-1,000,000 and attack angles (-10, 10) are given comparatively in Figure 4. In Figure 6, comparisons are made with two different turbulence models (Spalart-Allmaras, K-Epsilon), experimental calculations and the results of different studies in literature.

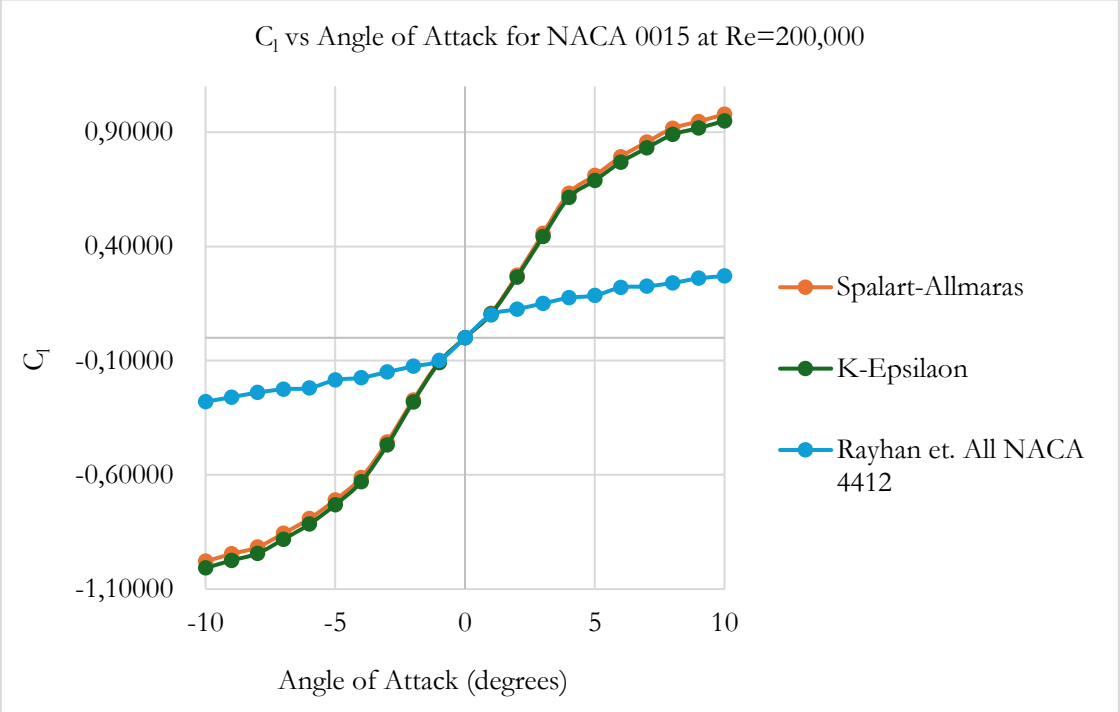

a1)

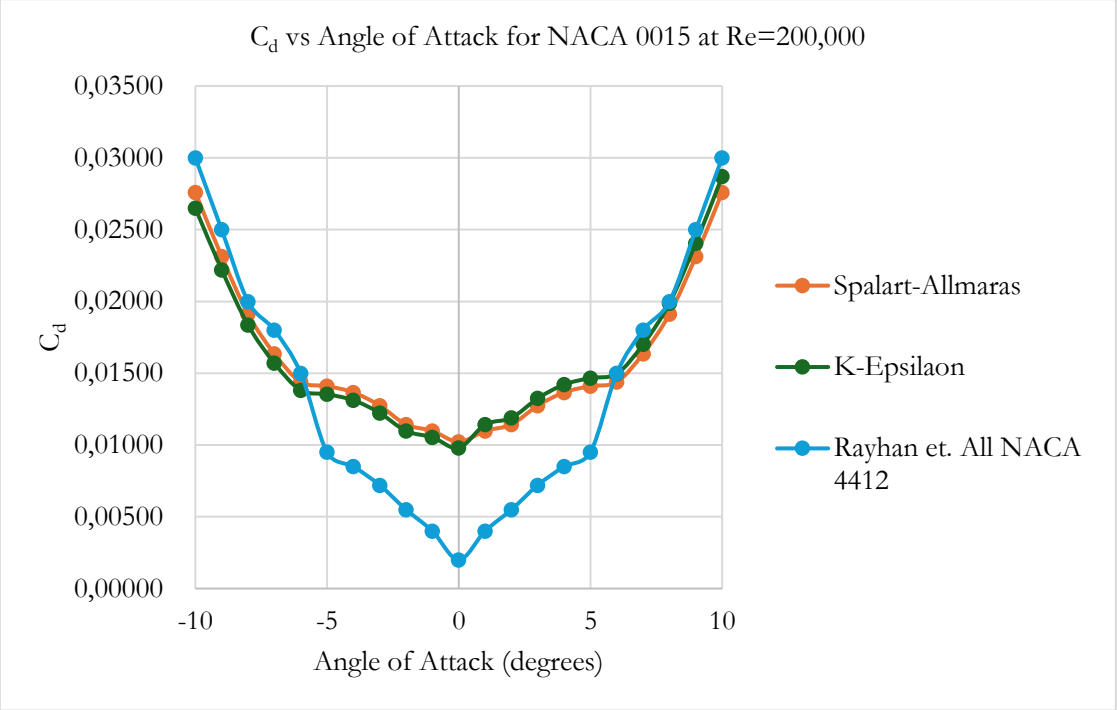
C_d vs Angle of Attack for NACA 0015 at Re=200,000
0,03500
0,03000
0,02500
0,02000
0,01500
0,01000
0,00500
0,00000
C_d
-10
-5
0
5
10
Angle of Attack (degrees)
Spalart-Allmaras
K-Epsilaon
Rayhan et. All NACA 4412

a2)

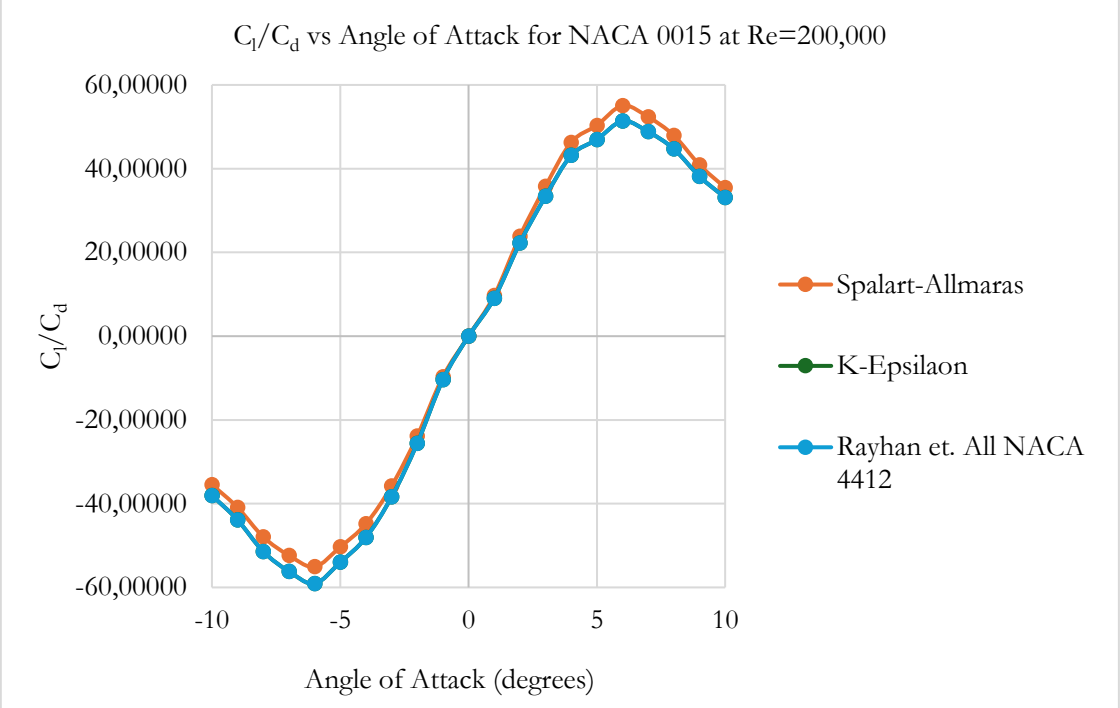
C_l/C_d vs Angle of Attack for NACA 0015 at Re=200,000
60,00000
40,00000
20,00000
0,00000
-20,00000
-40,00000
-60,00000
C_l/C_d
-10
-5
0
5
10
Angle of Attack (degrees)
Spalart-Allmaras
K-Epsilaon
Rayhan et. All NACA 4412

a3)

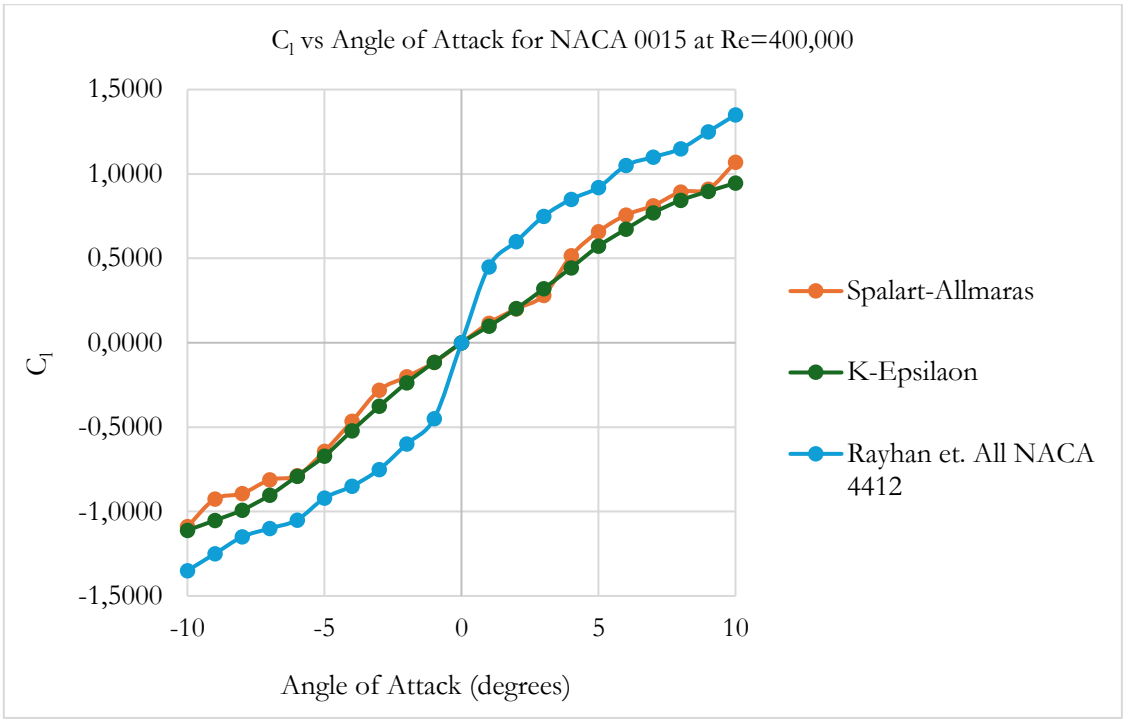
Cl vs Angle of Attack for NACA 0015 at Re=400,000
1,5000
1,0000
0,5000
0,0000
-0,5000
-1,0000
-1,5000
Cl
-10
-5
0
5
10
Angle of Attack (degrees)
Spalart-Allmaras
K-Epsilaon
Rayhan et. All NACA 4412

b1)

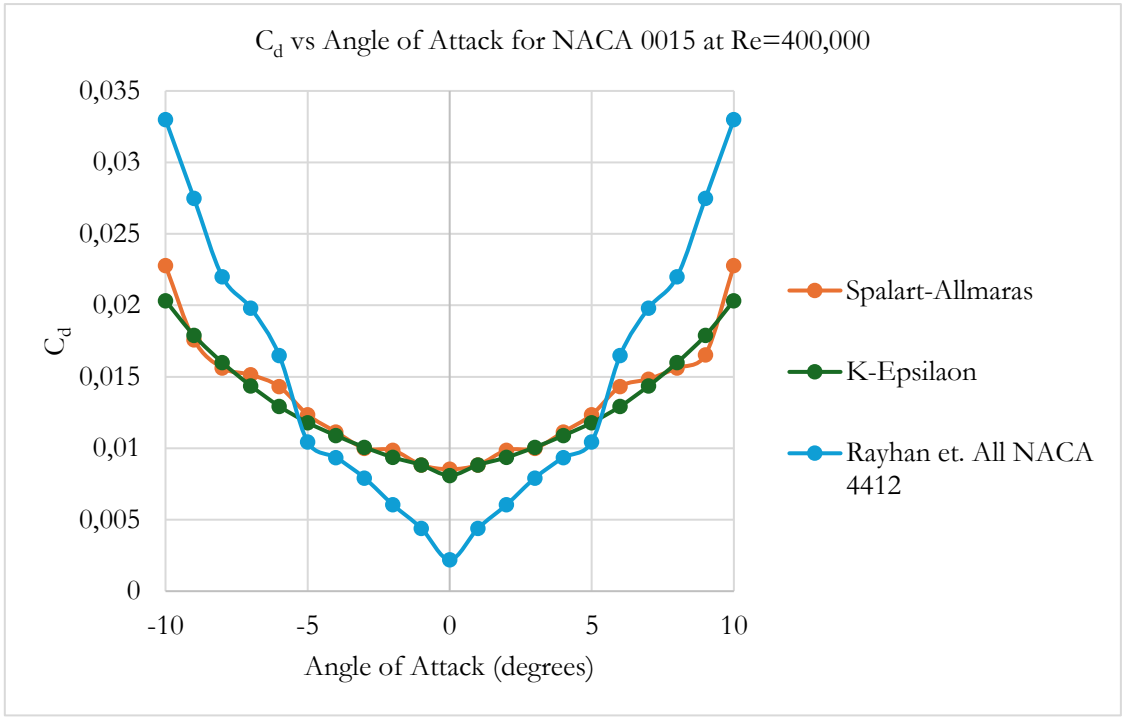
Cd vs Angle of Attack for NACA 0015 at Re=400,000
0,035
0,03
0,025
0,02
0,015
0,01
0,005
0
Cd
-10
-5
0
5
10
Angle of Attack (degrees)
Spalart-Allmaras
K-Epsilaon
Rayhan et. All NACA 4412

b2)

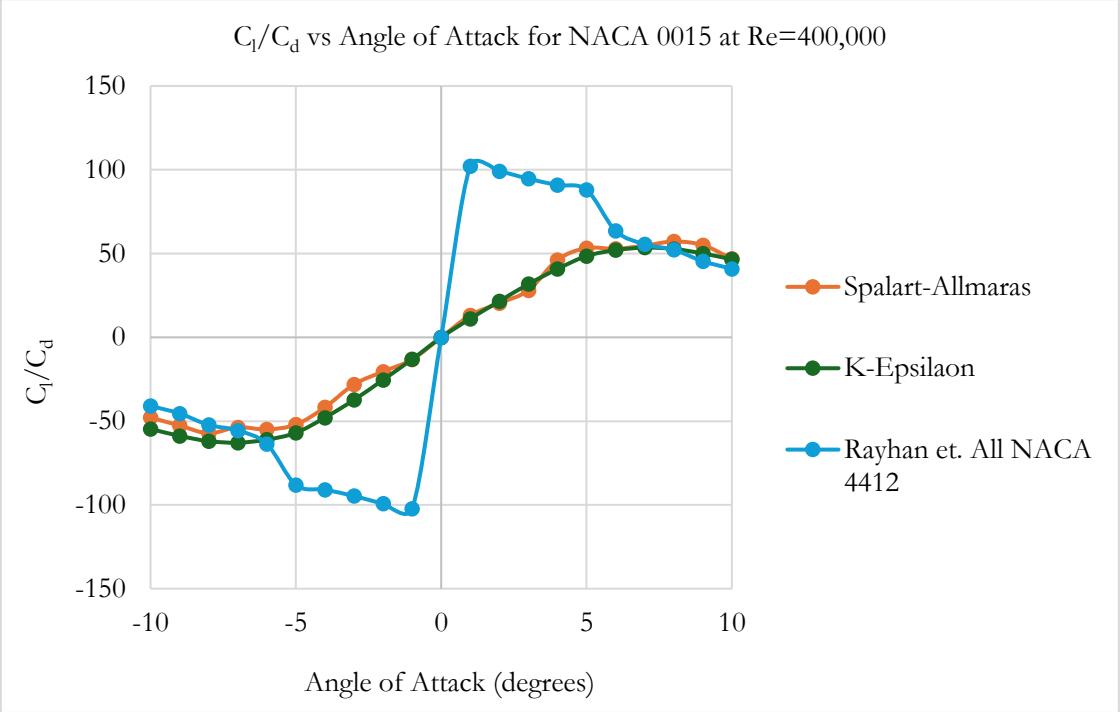
C_l/C_d vs Angle of Attack for NACA 0015 at Re=400,000
150
100
50
0
-50
-100
-150
-10
-5
0
5
10
C_l/C_d
Angle of Attack (degrees)
Spalart-Allmaras
K-Epsilaon
Rayhan et. All NACA 4412

b3)

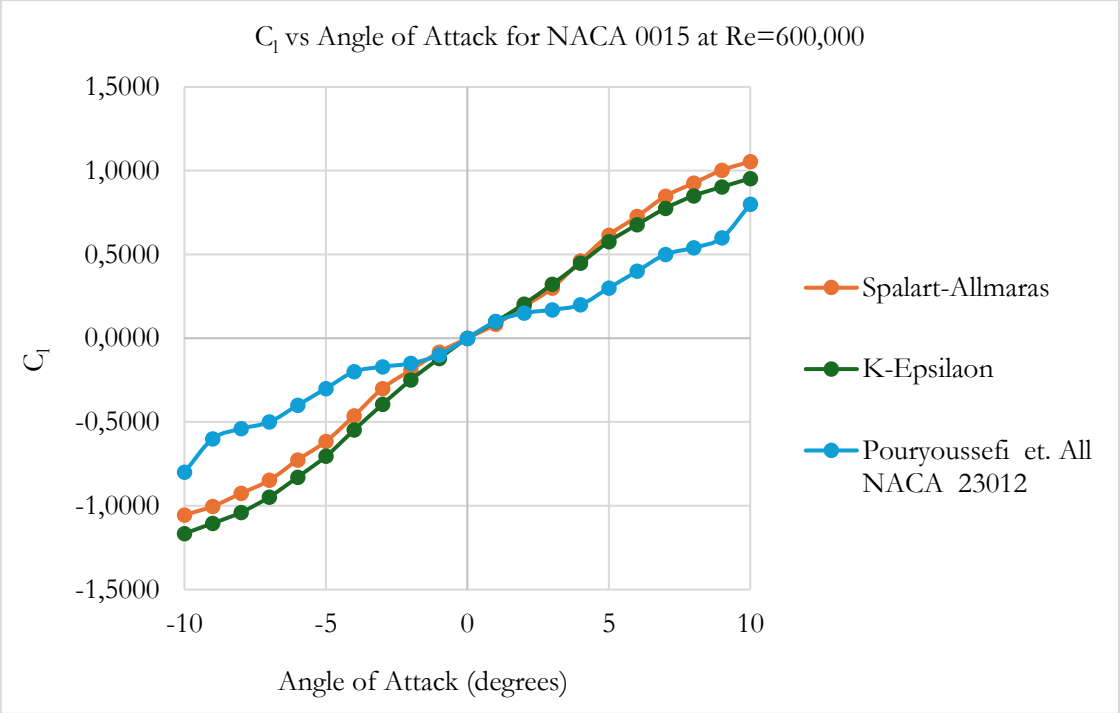
C_l vs Angle of Attack for NACA 0015 at Re=600,000
1,5000
1,0000
0,5000
0,0000
-0,5000
-1,0000
-1,5000
-10
-5
0
5
10
C_l
Angle of Attack (degrees)
Spalart-Allmaras
K-Epsilaon
Pouryoussefi et. All NACA 23012

c1)

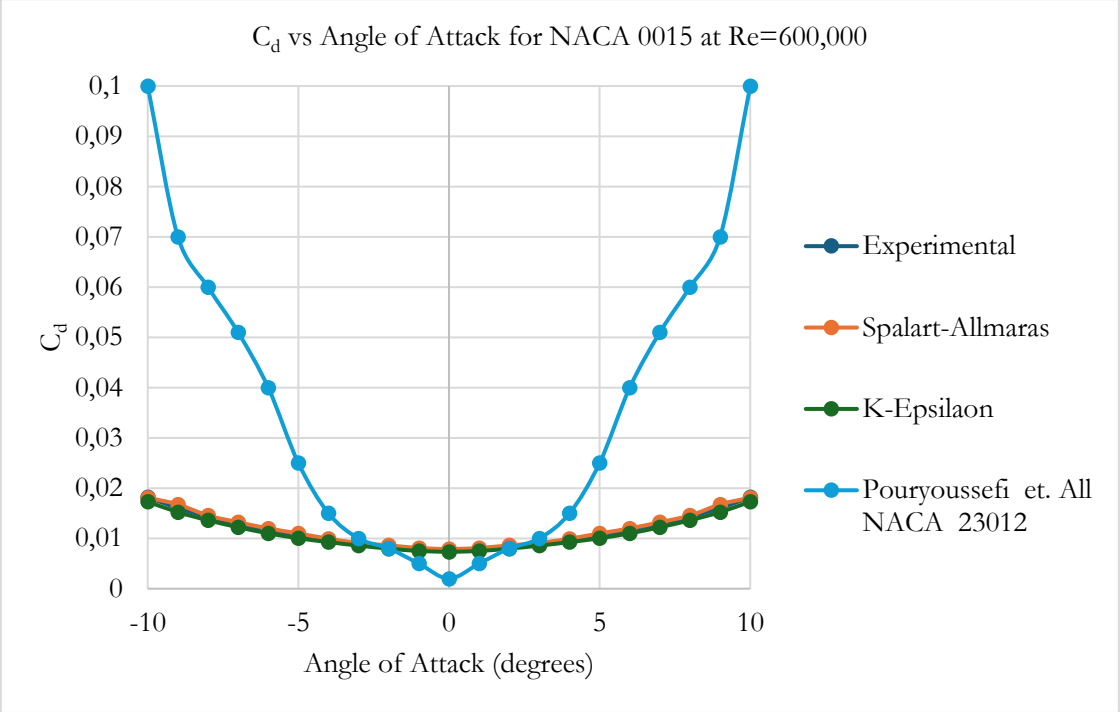
Cd vs Angle of Attack for NACA 0015 at Re=600,000
0,1
0,09
0,08
0,07
0,06
0,05
0,04
0,03
0,02
0,01
0
Cd
-10
-5
0
5
10
Angle of Attack (degrees)
Experimental
Spalart-Allmaras
K-Epsilaon
Pouryoussefi et. All NACA 23012

c2)

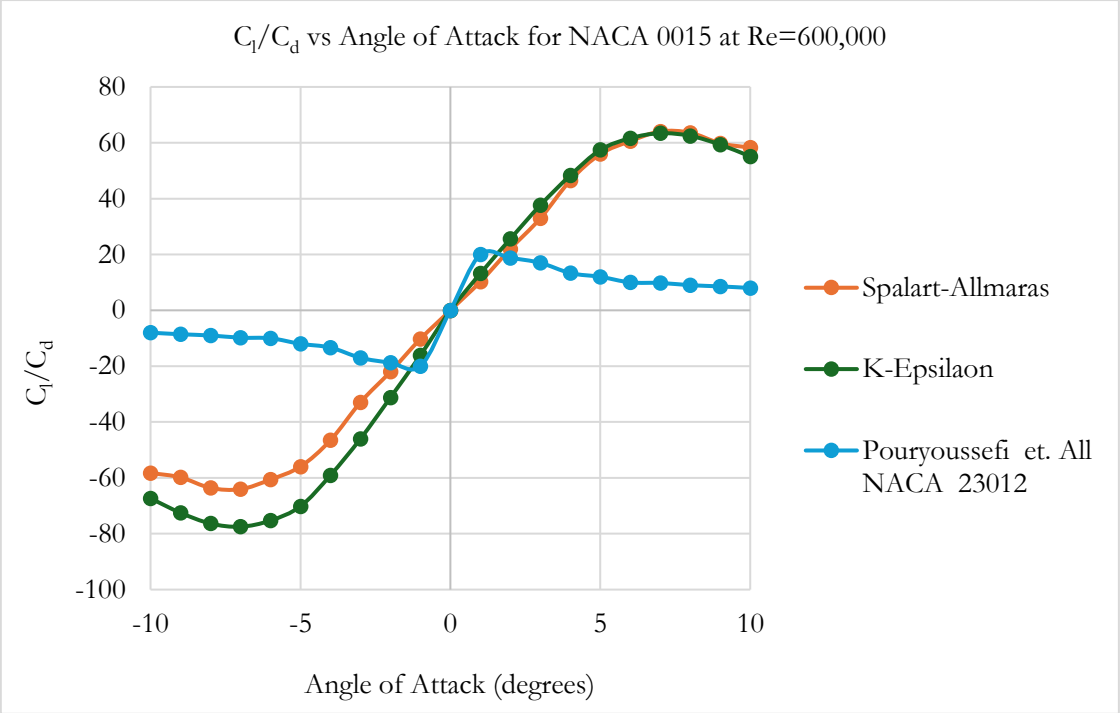
Cl/Cd vs Angle of Attack for NACA 0015 at Re=600,000
80
60
40
20
0
-20
-40
-60
-80
-100
Cl/Cd
-10
-5
0
5
10
Angle of Attack (degrees)
Spalart-Allmaras
K-Epsilaon
Pouryoussefi et. All NACA 23012

c3)

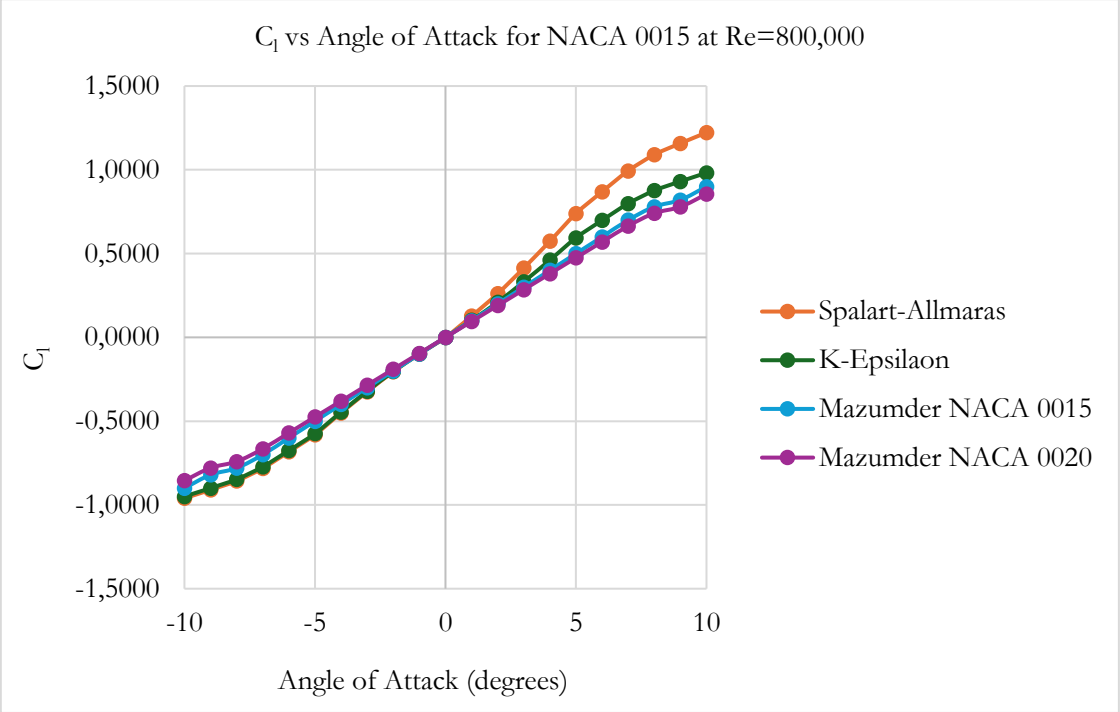
C_l vs Angle of Attack for NACA 0015 at Re=800,000
1,5000
1,0000
0,5000
0,0000
-0,5000
-1,0000
-1,5000
C_l
-10
-5
0
5
10
Angle of Attack (degrees)
Spalart-Allmaras
K-Epsilaon
Mazumder NACA 0015
Mazumder NACA 0020

d1)

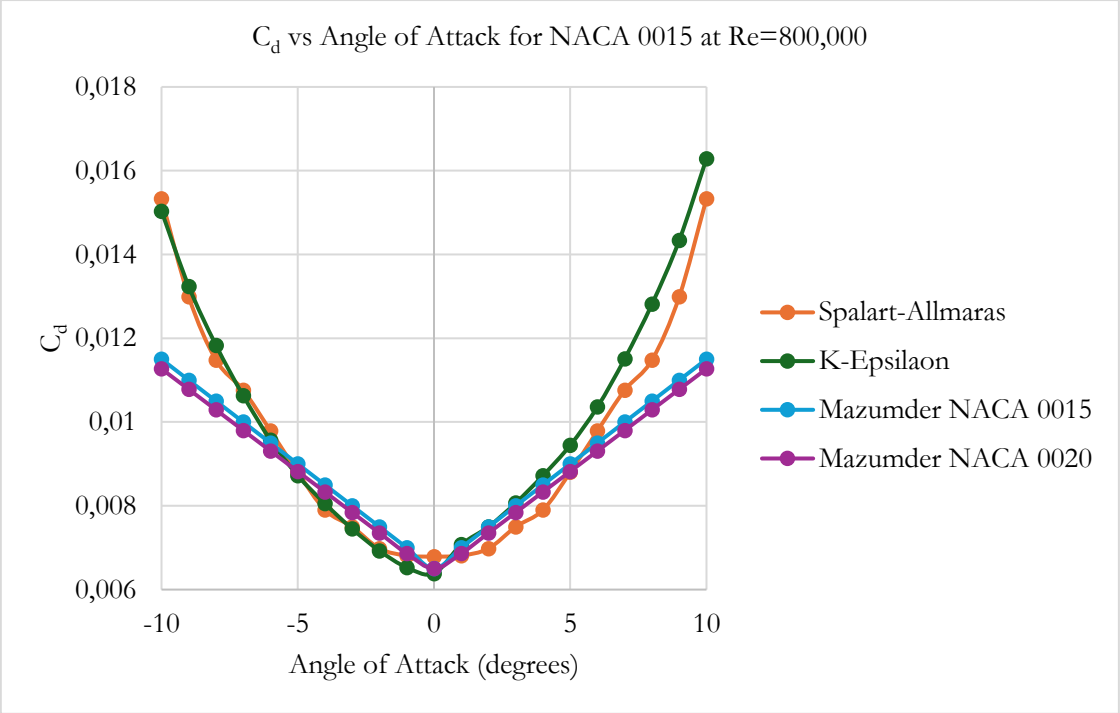
C_d vs Angle of Attack for NACA 0015 at Re=800,000
0,018
0,016
0,014
0,012
0,01
0,008
0,006
C_d
-10
-5
0
5
10
Angle of Attack (degrees)
Spalart-Allmaras
K-Epsilaon
Mazumder NACA 0015
Mazumder NACA 0020

d2)

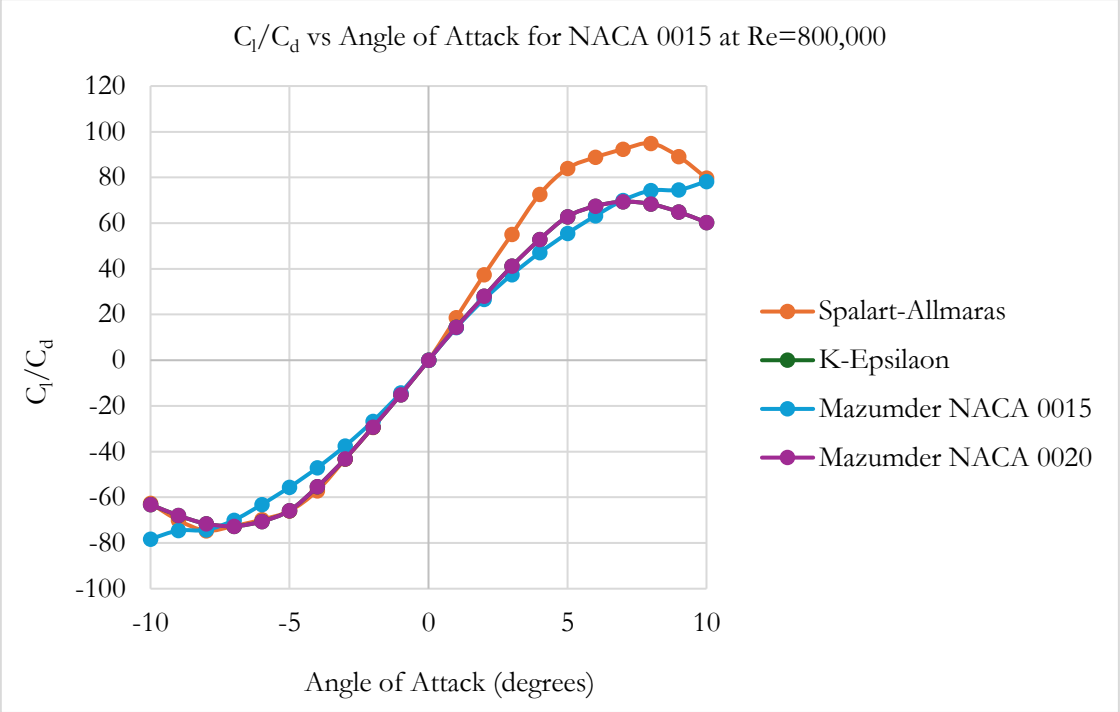
Cl/Cd vs Angle of Attack for NACA 0015 at Re=800,000
120
100
80
60
40
20
0
-20
-40
-60
-80
-100
-10
-5
0
5
10
Cl/Cd
Angle of Attack (degrees)
Spalart-Allmaras
K-Epsilaon
Mazumder NACA 0015
Mazumder NACA 0020

d3)

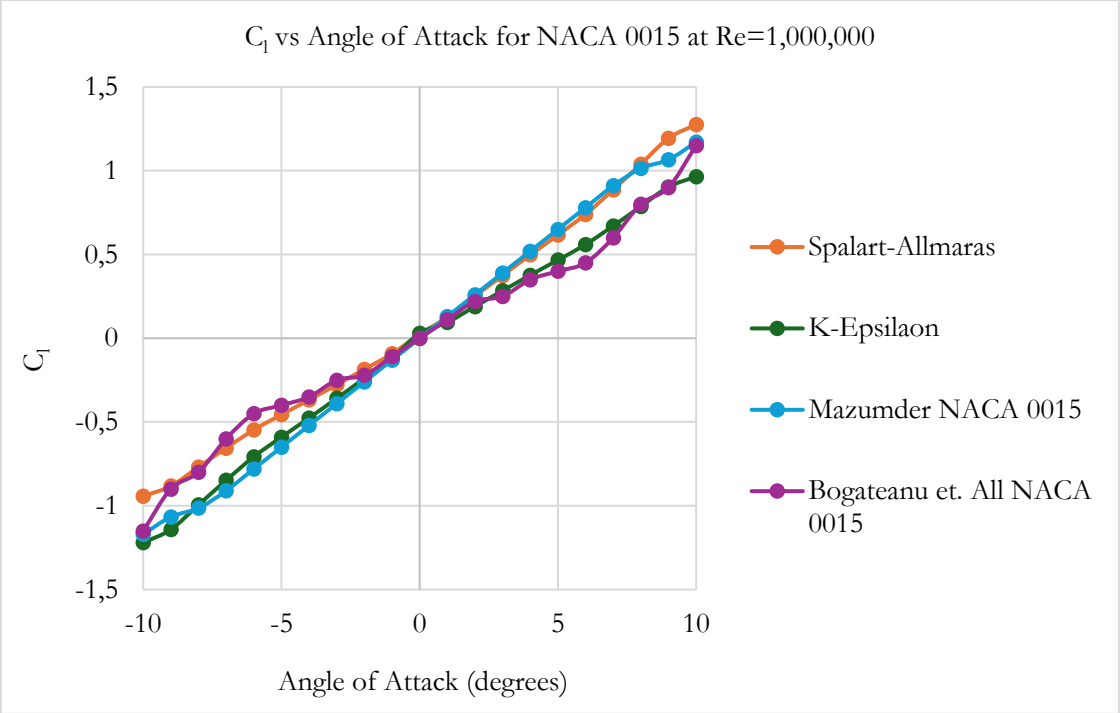
Cl vs Angle of Attack for NACA 0015 at Re=1,000,000
1,5
1
0,5
0
-0,5
-1
-1,5
-10
-5
0
5
10
Cl
Angle of Attack (degrees)
Spalart-Allmaras
K-Epsilaon
Mazumder NACA 0015
Bogateanu et. All NACA 0015

e1)

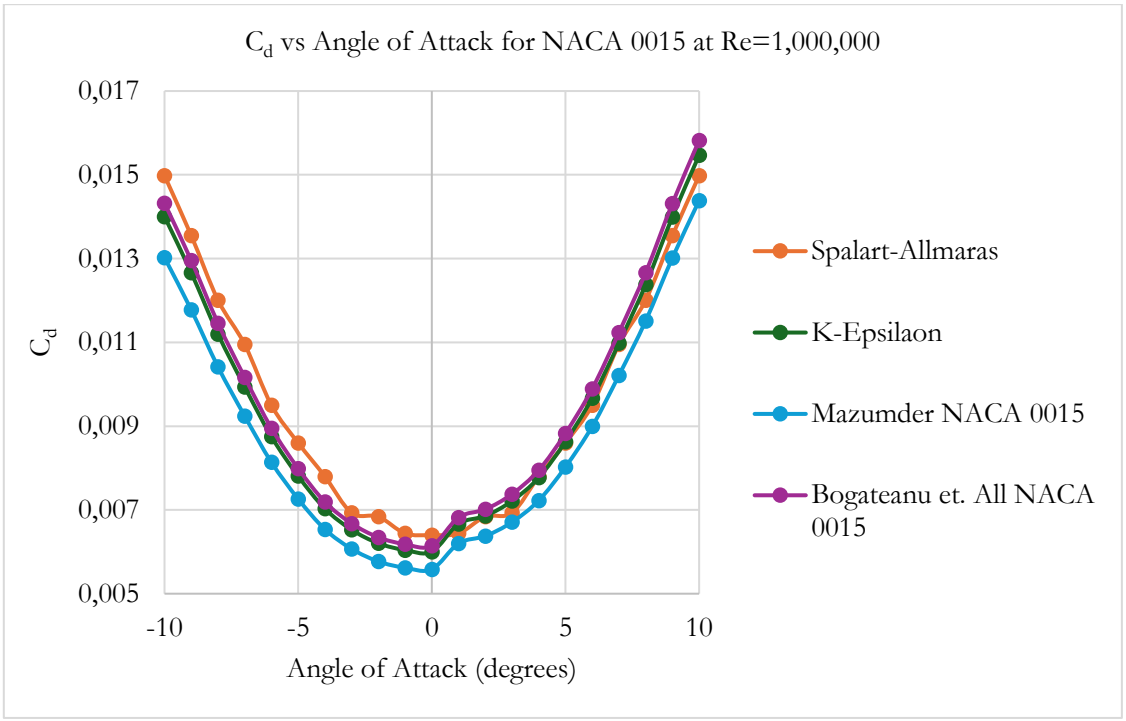

e2)

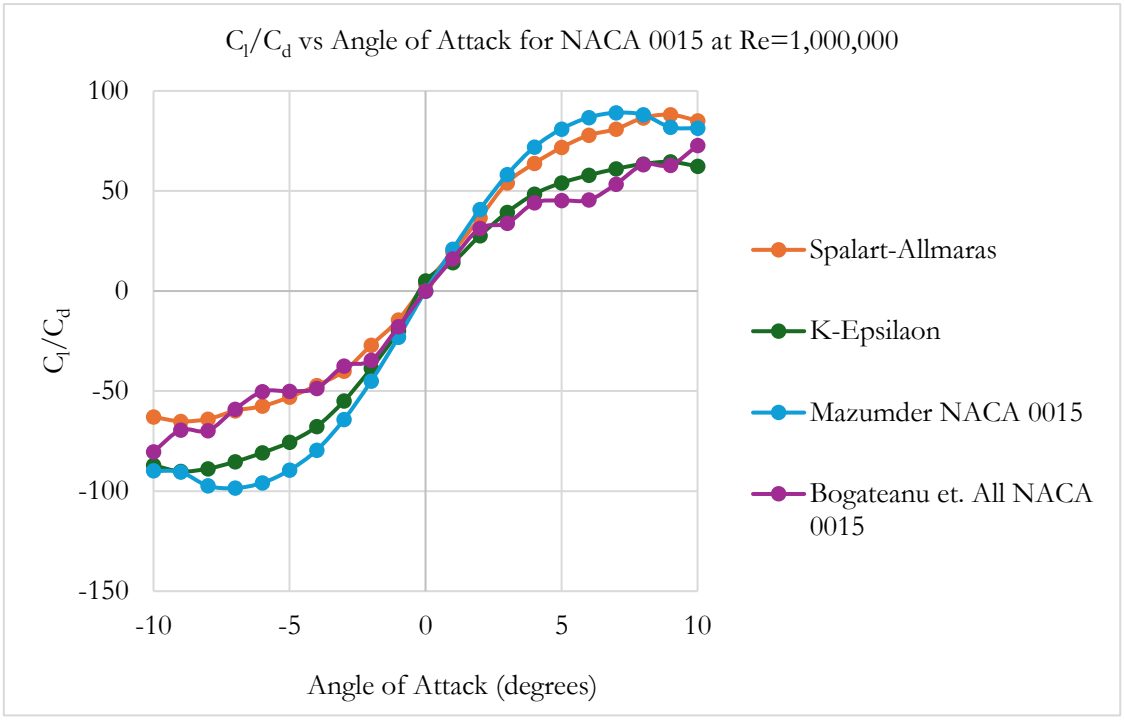

e3)

Figure 4. Aerodynamic Force Coefficients of the NACA 0015 Airfoil are a1) C_l, a2) C_d, a3) C_l/C_d for Re=200,000; b1) C_l, b2) C_d, b3) C_l/C_d for Re= 400,000; c1) C_l, c2) C_d, c3) C_l/C_d for Re= 600,000; d1) C_l, d2) C_d, d3) C_l/C_d for Re= 800,000; e1) C_l, e2) C_d, e3) C_l/C_d

Figure 4 illustrates that an increase in the angle of attack resulted in elevated aerodynamic force coefficients across all instances (C_l, C_d and C_l/C_d). The maximum lift coefficients (C_l) exhibited a linear increase up to $\alpha=8^0$, followed by a decline in the rate of increase. Based on observations from the graphs, a subsequent decline is observed, following a logarithmic trend. The experimental results are largely consistent with the Spalart-Almaras turbulence model. A distinct deviation is evident in the K-Epsilon turbulence model across all Re. Comparison of the experimental and simulation results using the Spalart-Allmaras turbulence model (for $\alpha = 8°$) shows varying trends

across different Reynolds numbers. Specifically, for Re=200,000, the simulation predicts a 3% decrease compared to the experimental data, while for Re=400,000, it shows a 4% increase. At Re=600,000, a slight decrease of 1% is observed, whereas for Re=800,000 and Re=1,000,000, the simulation results indicate significant increases of 12% and 15%, respectively. A comparable scenario led to a 5% reduction for Re=200,000, an 8% augmentation for Re=400,000, a 9% reduction for Re=600,000, a 10% reduction for Re=800,000, and a 13% reduction for Re=1,000,000 in the K-Epsilon turbulence model.

Figure 4 illustrates that the drag force coefficients (C_d) exhibit a logarithmic increase in relation to the angle of attack and Re. In this comparison of experimental data with data from alternative turbulence models, the most significant increase (for $\alpha=8^0$) is observed at Re=1,000,000 in the K-Epsilon turbulence model, amounting to 5%.

In addition, the results of the lift coefficient-drag ratio (C_l/C_d) examined at different Re and angles of attack are given in Figure 4 a3, b3, c3, d3 and e3. Here, this ratio, which increases linearly up to $\alpha=8^0$, exhibits a logarithmic decrease after $\alpha=8^0$. When the relevant graphs are examined, we can say that the experimental experiments and the Spalart-Almaras turbulence model are more compatible. As a result, while the C_l/C_d ratio is lower at low Re, the difference between them is calculated to be higher at high Re. The largest difference with a 17% decrease was observed in the K-Epsilon turbulence model with Re=1,000,000 (for $\alpha=8^0$), and the least difference with a 1% decrease was observed in the Spalart-Almaras turbulence model with Re=600,00. These data show that the NACA 0015 airfoil can improve the forward stall aerodynamic performance without significantly affecting the operating range. The data obtained agree with the literature.

The results show that the Spalart-Almaras turbulence model is more compatible (Mazumder, 2024), (Rayhan, Hossain, Mim, & Ali, 2024), (Pouryoussefi, Mirzaei, Nazemi, Fouladi, & Doostmahmoudi, 2016). In the light of the data obtained, the optimum aerodynamic values were determined as the angle of attack $\alpha=8^0$, Re=1,000,000.

3.2.2. Surface pressure and velocity

The distribution of the surface pressure coefficient across the upper and lower surfaces of the NACA 0015 airfoil, along with the comparison of velocity values, yields critical insights into the underlying mechanism. Figure 5 presents the surface pressure distribution curve.

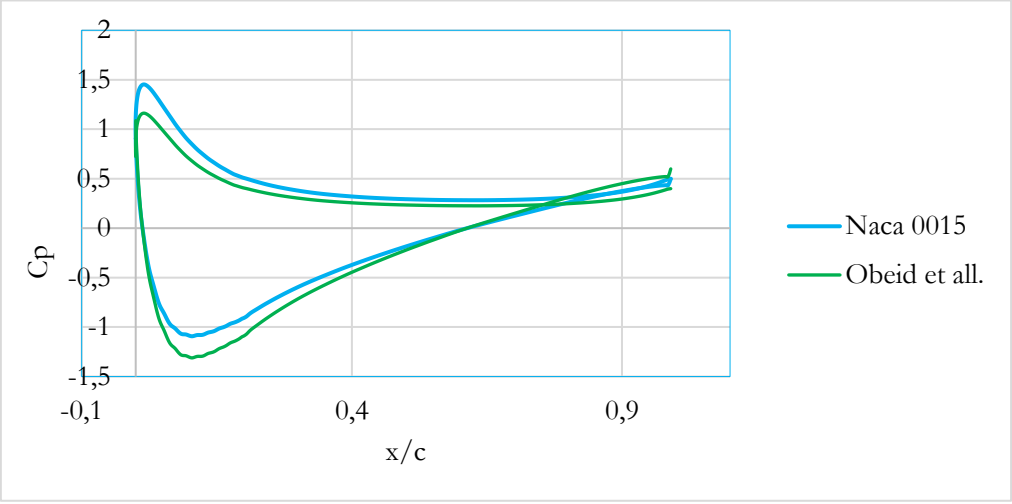

Figure 5. Pressure Coefficient Distribution Curve along the Upper and Lower Surfaces for Angle of Attack $\alpha=8^0$

At low angles of attack, the C_p distribution exhibits negative pressure at the apex. After this juncture, the pressure coefficient progressively escalates along the chord. It attains its peak value when C_p=-1.1 at the stop line. Figure 6 illustrates that the flow remains adhered to the suction surface before commencing separation. The pressure coefficient increases as the flow on the lower surface decelerates, while it decreases as the flow speed on the upper surface accelerates. Consequently, as the pressure differential between the lower and upper surfaces escalates, the lift force correspondingly increases. The acquired values align with the literature (Obeid, Jha, & Ahmadi, 2017).

Figure 6 shows the velocity contour generated on the NACA 0015 airfoil. The impact of the variation in pressure differential between the lower and upper surfaces is distinctly evident from the alterations in velocity depicted on the velocity contour. This impact is seen in Figure 6b.

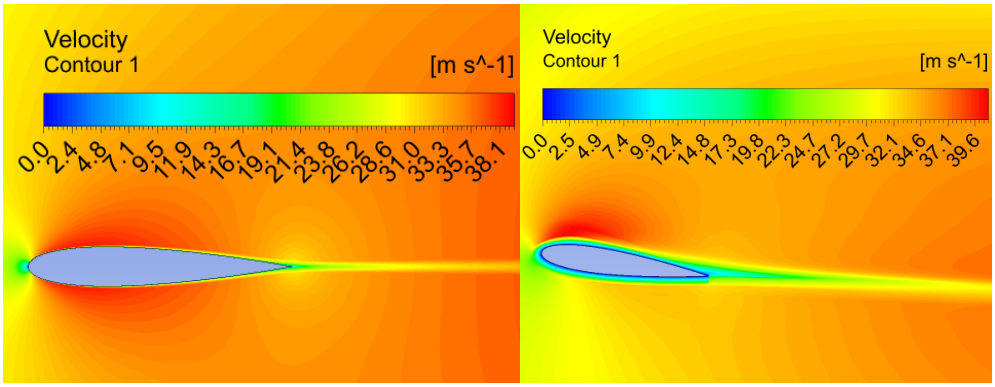

a) b)

Figure 6. Velocity Magnitude Contour of NACA 0015 Airfoil for Angle of Attack a) $\alpha=0^0$ and b) $\alpha=8^0$

In Figure 6a, the average speed values in the upper and lower regions of the wing profile are 36.5 m/s. In Figure 6b, the average speed values in the upper and lower regions of the wing profile are determined to be 29.6 m/s and 18.1 m/s, respectively (The average speed is calculated along a line). In Figure 6a, the equivalence of average speed values in the upper and lower regions can be attributed to an angle of attack of 0 degrees. In Figure 5, the pressure differential between the upper and lower sections of the wing profile also influenced the average velocity values.

4. CONCLUSION

This study analyzes and compares the aerodynamic performance of the NACA 0015 airfoil. An inner slot with a chord length of 1 meter is chosen. CFD simulations are conducted at low Re (200,000, 400,000, 600,000, 800,000 and 1,000,000) and varying angles of attack ($\alpha=-10^0$, 10^0). Two distinct turbulence models, Spalart-Allmaras and K-Epsilon are employed in the simulations. The studies utilizing the Spalart-Allmaras turbulence model demonstrate enhanced performance. The findings derived from the study are as follows:

- The increase of the angle of attack led to an elevation in the aerodynamic force coefficients across all instances (C_l, C_d and C_l/C_d). In the conducted studies, the angle of attack was constrained to $\alpha=-10^0$, 10^0. Literature studies indicate a reduction in force coefficients, particularly after $\alpha=15^0$.
- Upon evaluation of the results, optimal aerodynamic performance is noted at Re=1,000,000 using the Spalart-Allmaras turbulence model.
- The pressure coefficient (C_p) on the upper and lower surfaces of the airfoil at an angle of attack $\alpha=8^0$ was computed. A negative pressure coefficient (maximum $C_p=-1.1$) was observed on the upper surface, whereas a positive pressure coefficient (maximum $C_p=1.5$) was detected on the lower surface. The disparity in pressure coefficients on the surfaces also influenced the average velocity on the upper and lower surfaces. The average speed on the upper surface at an angle of attack $\alpha=8^0$ was determined to be 29.6 m/s, while the average speed on the lower surface was calculated to be 18.1 m/s.

The results indicate that the NACA 0015 airfoil could be an effective means to enhance aerodynamic performance. In forthcoming research, we intend to fabricate this airfoil in an experimental setting and conduct a comprehensive simulation of the wing. We intend to commercialize the study based on the results acquired from testing this airfoil in an experimental wind turbine.

ETHICAL STATEMENT & GENERAL STATEMENTS

This article meets the standards of research and publication ethics.

AUTHORS' CONTRIBUTIONS

All authors have read and approved the final manuscript.

FUNDING

Not applicable.

AVAILABILITY OF DATA AND MATERIALS

Not applicable.

COMPETING INTERESTS

The authors declare that they have no competing interests.

REFERENCES

Abed, K. N. (2023). The effect of location and shape of vortex generators on aerodynamic characteristics of a NACA 4415 airfoil. *Al-Nahrain Journal for Engineering Sciences, 26*(3), pp. 198–204. doi:10.29194/NJES.26030198

Abramova, K. A., Alieva, D. A., Sudakov, V. G., & Khrabrov, A. N. (2024). Modeling of the unsteady aerodynamic characteristics of the NACA 0015 airfoil from the data of numerical calculations of the flow. *Fluid Dynamics, 59*(1), s. 130–44. doi:10.1134/S0015462823602929

Ai, Q., Jawahar, H. K., & Azarpeyvand, M. (2016). Experimental investigation of aerodynamic performance of airfoils fitted with morphing trailing edges. *54th AIAA Aerospace Sciences Meeting.* doi:10.2514/6.2016-1563

Almusawi, M., Rishack, Q., & Al-fahham, M. (2022). Effect of spanwise semicircular groove on NACA 0012 airfoil. *Basrah Journal for Engineering Science, 22*(2), pp. 23–26. doi:10.33971/bjes.22.2.4

Arif, M. S., Afzal, M. J., Javaid, F., Tayyaba, S., Ashraf, M. W., Ishraque, G. F., & Hossain, M. K. (2022). Laminar flow analysis of NACA 4412 airfoil through ANSYS fluent. *Proceedings of International Exchange and Innovation Conference on Engineering & Sciences (IEICES), 8*, pp. 394–399. doi:10.5109/5909123

Ayaz Ümütlü, H. C., Kiral, Z., & Karadeniz, Z. H. (2023). Experimental investigation of NACA 4415 airfoil using vibration data for stall detection. *Aircraft Engineering and Aerospace Technology, 95*(10), pp. 1551–1559. doi:10.1108/AEAT-03-2023-0077

Bangga, G., Hutani, S., & Heramarwan, H. (2021). The effects of airfoil thickness on dynamic stall characteristics of high-solidity vertical axis wind turbines. *Advanced Theory and Simulations, 4*(6). doi:10.1002/adts.202000204

Berger, M., Raffeiner, P., Senfter, T., & Pillei, M. (2024). A comparison between 2D DeepCFD, 2D CFD simulations and 2D/2C PIV measurements of NACA 0012 and NACA 6412 airfoils. *Engineering Science and Technology, an International Journal*(57). doi:10.1016/j.jestch.2024.101794

Bogateanu, R., Dumitrache, A., Dumitrescu, H., & Stoica, C. I. (2014). Reynolds number effects on the aerodynamic performance of small VAWTs. *Scientific Bulletin-University Politehnica of Bucharest, 76*(1). Retrieved Feb 21, 2025, from https://www.scientificbulletin.upb.ro/rev_docs_arhiva/full084_828545.pdf

Dell'Orso, H., & Amitay, M. (2018). Parametric investigation of stall cell formation on a NACA 0015 airfoil. *AIAA Journal, 56*(8), pp. 3216–3228. doi:10.2514/1.J056850

Feng, Y. (2023). A numerical study on the optimization of an airfoil design. *Theoretical and Natural Science, 11*(1), pp. 199–206. doi:10.54254/2753-8818/11/20230408

Gopalarathnam, A., & Selig, M. S. (2001). Low-speed natural-laminar-flow airfoils: Case study in inverse airfoil design. *Journal of Aircraft, 38*(1), pp. 57–63. doi:10.2514/2.2734

Hassan, M. I., Andan, A. D., Asrar, W., & Sapardi, M. A. (2023). Large Eddy simulation of low Reynolds number flow around a NACA0015 airfoil with modified trailing edges. *Journal of Advanced Research in Applied Mechanics, 112*(1), pp. 57–79. doi:10.37934/aram.112.1.5779

He, Y., & Agarwal, R. K. (2014). Shape optimization of NREL S809 airfoil for wind turbine blades using a multiobjective genetic algorithm. *International Journal of Aerospace Engineering, 2014*, pp. 1–13. doi:10.1155/2014/864210

Hu, H., & Tamai, M. (2008). Bioinspired corrugated airfoil at low Reynolds numbers. *Journal of Aircraft, 45*(6), pp. 2068–2077. doi:10.2514/1.37173

Jawahar, K. H., Q. A., & Azarpeyvand, M. (2018). Aerodynamic and aeroacoustic performance of airfoils fitted with morphing trailing-edges. *2018 AIAA/CEAS Aeroacoustics Conference*. doi:10.2514/6.2018-2815

Julian, J., Siswanto, S. A., Wahyuni, F., & Bunga, N. T. (2023). Analysis of the use of bio flap on NACA 4415 with numerical methods. *Jurnal Asiimetrik: Jurnal Ilmiah Rekayasa & Inovasi*, pp. 251–262. doi:10.35814/asiimetrik.v5i2.4768

Kaya, A. F. (2024). Investigation of a rib structure effect on the aerodynamic performance of a plain flapped symmetrical airfoil. *Journal of Polytechnic, 27*(3), pp. 967-974. doi:10.2339/politeknik.1159822

Launder, B. E. (1972). *Lectures in Mathematical Models of Turbulence.* Academic Press.

Li, L., Sherwin, S. J., & Bearman, P. W. (2002). A moving frame of reference algorithm for fluid/structure interaction of rotating and translating bodies. *International Journal for Numerical Methods in Fluids, 38*(2), pp. 187–206. doi:10.1002/fld.216

Li, S., Li, Y., Yang, C., Zhang, X., Wang, Q., Li, D., . . . Wang, T. (2018). Design and testing of a LUT airfoil for straight-bladed vertical axis wind turbines. *Applied Sciences, 8*(11). doi:10.3390/app8112266

Liu, Y., Lu, L., Fang, L., & Gao, F. (2011). Modification of Spalart–Allmaras model with consideration of turbulence energy backscatter using velocity helicity. *Physics Letters A, 375*(24), pp. 2377–2381. doi:10.1016/j.physleta.2011.05.023

Mazumder, H. M. (2024). CFD Analysis of NACA Airfoils for Wind Turbine and Aerospace Applications at Low Reynolds Numbers. Bangladesh University of Engineering and Technology (BUET).

Medjroubi, W., Stoevesandt, B., Carmo, B., & Peinke, J. (2011). High-order numerical simulations of the flow around a heaving airfoil. *Computers & Fluids, 51*(1), pp. 68–84. doi:10.1016/j.compfluid.2011.07.015

Nepal, S., Qijun, Z., Bo, W., Kamruzzaman, M., & Adhikari, S. (2023). Aerodynamic simulation and optimization of micro aerial vehicle rotor airfoil at low Reynolds number. *Asian Review of Mechanical Engineering , 12*(1), pp. 24–38. doi:10.51983/arme-2023.12.1.3670

Obeid, S., Jha, R., & Ahmadi, G. (2017). RANS simulations of aerodynamic performance of NACA 0015 flapped airfoil. *Fluids, 2*(1). doi:10.3390/fluids2010002

Pack Melton, L., Hannon, J., Yao, C.-S., & Harris, J. (2008). Active flow control at low Reynolds numbers on a NACA 0015 airfoil. *26th AIAA Applied Aerodynamics Conference*. doi:10.2514/6.2008-6407

Pouryoussefi, S. G., Mirzaei, M., Nazemi, M.-M., Fouladi, M., & Doostmahmoudi, A. (2016). Experimental study of Ice accretion effects on aerodynamic performance of an NACA 23012 airfoil. *Chinese Journal of Aeronautics, 29*(3), pp. 585-595. doi:10.1016/j.cja.2016.03.002

Rayhan, A. M., Hossain, M. S., Mim, R. H., & Ali, M. (2024). Computational and experimental study on the aerodynamic performance of NACA 4412 airfoil with slot and groove. *Heliyon , 10*(11). doi:10.1016/j.heliyon.2024.e31595

Saeed, F., Paraschivoiu, I., Trifu, O., Hess, M., & Gabrys, C. (2011). Inverse airfoil design method for low-speed straight-bladed Darrieus-type VAWT applications. *Wind Engineering, 35*(3), pp. 357–67. doi:10.1260/0309-524X.35.3.357

Sato, M., Asada, K., Nonomura, T., Kawai, S., & Fujii, K. (2017). Large-Eddy simulation of NACA 0015 airfoil flow at Reynolds number of 1.6×106. *AIAA Journal, 55*(2), pp. 673–679. doi:10.2514/1.J054963

Siauw, W. L., Bonnet, J. P., Tensi, J., Cordier, L., Noack, B. R., & Cattafesta, L. (2010). Transient dynamics of the flow around a NACA 0015 airfoil using fluidic vortex generators. *International Journal of Heat and Fluid Flow, 31*(3), pp. 450–459.

Spalart, P., & Allmaras, S. (1992). A one-equation turbulence model for aerodynamic flows. *30th Aerospace Sciences Meeting and Exhibit*. doi:10.2514/6.1992-439

Sun, H. (2011). Wind turbine airfoil design using response surface method. *Journal of Mechanical Science and Technology, 25*(5), pp. 1335–40. doi:10.1007/s12206-011-0310-6

Tanürün, H. E., Akın, A. G., Acır, A., & Şahin, İ. (2024). Experimental numerical investigation of roughness structure in wind turbine airfoil at low Reynolds number. *International Journal of Thermodynamics, 27*(3), pp. 26–36. doi:10.5541/ijot.1455513

Zulkefli, N. F., Ahamat, M. A., Mohd Safri, N. F., Mohd Nur, N., & Mohd Rafie, A. S. (2019). Lift enhancement of NACA 4415 airfoil using biomimetic shark skin vortex generator. *International Journal of Recent Technology and Engineering (IJRTE) , 8*(4), pp. 9231–9234. doi:10.35940/ijrte.D9222.118419